ACS OMEGA

Open Access

http://pubs.acs.org/journal/acsodf

Article

Comprehensive Assessment and Optimization of a Middle-Arch Dual-Channel Municipal Solid Waste Incinerator Using Numerical Simulation Methods

Hongquan Zhou, Ruizhi Zhang,* Linzheng Wang, and Yonghao Luo

Cite This: *ACS Omega* 2024, 9, 42010−42026

Read Online

ACCESS | Metrics & More | Article Recommendations

ABSTRACT: The present study focuses on a middle-arch dual-channel municipal solid waste (MSW) incinerator facing issues of high NO_x emission and overheating. To address these problems and optimize the incinerator, an advanced numerical simulation method was employed to comprehensively assess its bed combustion, freeboard combustion, and NO_x emission characteristics. A multiphase fuel bed model considering large-particle characteristics of MSW was developed, coupled with a three-dimensional (3D) model for combustion in freeboard. The analysis revealed that the observed issues stem from multiple factors, including primary-to-secondary air ratio, flame propagation in bed, release of volatiles from bed, and distribution and mixing of components in freeboard. Reducing the proportion of primary air and correspondingly increasing secondary air effectively alleviated the localized overheating in the furnace and reduced NO_x emission. Further adjustments to the distribution of primary air in three stages delaying air supply toward the burnout stage, together with the decrease in the grate movement speed, can better control the amount and speciation of N released from the bed. Implementing a counterflow mixing strategy with NH_3 in the front channel and NO in the rear channel can greatly reduce the original NO_x emission concentration to 95.94 mg/(N·m^3), as predicted by a numerical simulation. Subsequent practical adjustments to an actual incinerator led to notable improvements, clearly optimizing the localized high-temperature issues at various locations, especially the front channel suffering severe slagging problems, with the temperature reduced from 1118 to 957 °C. Meanwhile, NO_x emission concentration decreased from 200 mg/(N·m^3) to around 50 mg/(N·m^3), with no negative effect on the boiler load.

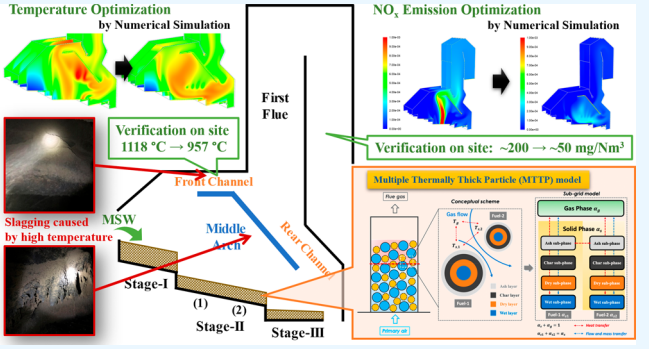

1. INTRODUCTION

China's economic expansion has driven rapid urbanization, resulting in a marked rise in municipal solid waste (MSW) generation.[1] While landfill was historically the predominant technique, it is facing issues such as soil contamination from leachate and accumulation of aged refuse.[2] Incineration, on the other hand, is noted for its high efficiency and substantial volume reduction.[3] The China Statistical Yearbook 2023 reports a total of 583 MSW incineration plants, with incineration now handling around 70% of the country's MSW, making it the leading treatment method. In particular, the incineration of MSW through grate-firing furnaces is the mainstream technology in modern waste management strategies. This technology has proven its adaptability and efficiency in handling varying waste compositions, gaining widespread adoption.[4] Modern MSW incineration technology enables the efficient thermal processing of heterogeneous waste materials, converting them into heat and power while significantly reducing the mass and volume of waste that would otherwise occupy landfill spaces. However, the quest for operational optimization in MSW incineration systems is currently driven by the pressing need to improve combustion efficiency and reduce the environmental impact.[5]

The environmental footprint of MSW incineration, particularly concerning the emission of nitrogen oxides (NO_x), remains a critical concern.[6] The predominant emissions from municipal solid waste (MSW) incinerators are fuel-derived NO_x.[7] The formation of fuel NO_x is closely related to the combustion temperature and the availability of oxygen during the in-furnace incineration processes.[8] Therefore, to meet stringent burnout standards and reduce NO_x emissions, one effective strategy is to lower the oxygen levels in the combustion environment, and precise control over the

Received: July 31, 2024
Revised: August 30, 2024
Accepted: September 4, 2024
Published: September 24, 2024

combustion environment is essential to suppress NO_x formation. This includes optimizing parameters such as air supply, mixing conditions, residence time, and temperature profiles within the combustion chamber.[9] However, reports on successful NO_x reduction through air supply optimization in industrial-scale waste incineration facilities are scarce. It must be noted that the combustion process in grate furnaces is inherently complex and presents significant challenges regarding operational optimization, which calls for the development of advanced quantitative analysis tools.

In recent years, the advancement of numerical modeling, especially with computational fluid dynamics (CFD), has empowered researchers and engineers to comprehensively investigate the MSW incineration processes.[10] The advanced CFD modeling approaches allow for the simulation of multiphysical and chemical processes, thereby providing insights that can lead to the optimization of design and operational parameters.[11] By harnessing the predictive capabilities of CFD, it is possible to explore a wide range of design modifications and operational adjustments without the need for costly and time-consuming trials in real furnaces. For instance, Xia et al.[12] used a two-fluid model to simulate a moving grate waste incinerator, successfully predicting temperature and gas species distributions, confirmed by real measurements. The research also analyzed particle properties and the impact of waste throughput on the incineration efficiency. Yang et al.[7] established numerical models of a 350 tons/day MSW incinerator to examine how optimizing air supply, including the adjustment of primary and secondary air (SA) ratios, distribution of secondary air guns, and overfired air supply methods, could enhance NO_x reduction in an MSW incinerator. Findings showed improved combustion and flow characteristics, leading to reduced initial NO_x formation and increased efficiency of selective non-catalytic reduction (SNCR)-based NO_x removal. Yan et al.[13] conducted numerical simulations to investigate how varying primary air (PA) temperatures influence an incinerator's combustion. They found that higher primary air temperatures increased the rates of water evaporation and volatile matter release. This intense volatilization, however, caused a localized high temperature in multiple areas of the incinerator. Such research underscores the potential of CFD in exploring design modifications and operational adjustments without the extensive costs associated with physical trials. In general, although many studies have begun to employ advanced numerical simulation techniques to analyze the complex combustion processes within MSW grate furnaces, and some investigations have explored the trends in NO_x emissions under varying operational conditions, most research predominantly focused on the gas-phase combustion processes within the furnace chamber.[7,8,14] There is still a lack of targeted analysis on how these different conditions affect combustion in the fuel bed and consequently how the distribution of NO_x and their precursors will be altered on the top surface of the bed, which are critical intermediary mechanisms that remain insufficiently understood. Consequently, the regulatory mechanisms of combustion in bed and freeboard, as well as NO_x emissions, have yet to be fully delineated with clarity for better design and control of these furnaces.

The present study focuses on a middle-arch dual-channel MSW incinerator that has a unique arched and two-channel gas flow structure.[15] Despite its distinctive design, the incinerator is still facing issues such as high initial NO_x emission and overheating when processing high-calorific wastes under common operation conditions, thus requiring optimization. To address these problems and optimize the incinerator's performance, advanced numerical simulation method is employed to comprehensively assess bed combustion, freeboard combustion, and pollutant emission characteristics of the incinerator both before and after optimization. To accurately simulate the MSW incineration process, a multiphase fuel bed combustion model considering the large-particle characteristics of MSW is developed, and coupled with a three-dimensional (3D) CFD model for combustion in the freeboard of the furnace. This integrated approach enables quantitative analysis of bed combustion, freeboard combustion, and NO_x formation and reduction mechanisms. The model is validated against on-site data obtained from the middle-arch MSW incinerator to ensure its reliability and accuracy.

2. MODEL ESTABLISHMENT

2.1. Model Framework and Major Assumptions. The numerical simulation of grate boilers requires comprehensive modeling that captures both combustion within the fuel bed on the grate and the subsequent gas-phase combustion in the freeboard. In this work, the combustion processes in the grate furnace were calculated using a state-of-the-art comprehensive CFD model, which included a multiphase fuel bed model with thermally thick particle treatment and a gas-phase freeboard combustion model. For the gas-phase combustion, ANSYS Fluent 2020 R2 was employed, with the configuration of turbulence, species transport, and radiation models referencing Hoang et al.'s work.[16] This section focuses primarily on elucidating the fuel bed model.

Key assumptions adopted in the model[17,18] are outlined as follows:

(1) The fuel bed is treated as a porous medium with a fixed void fraction. This assumption simplifies the complex interactions within the fuel bed, allowing for a manageable computational model. Besides, a volume change model is employed to capture the reduction in solid phase volume.

(2) Fuel particles are modeled as thermally thick and spherical-equivalent, subdivided into four distinct layers: a wet layer, a dry layer, a char layer, and an ash layer. This assumption simplifies the geometry and thermal behavior of the particles, distinct processes such as drying, devolatilization, and char combustion occur respectively in the wet, dry, and char layers, enabling detailed analysis of these processes.

(3) Within the porous medium, each layer of particle is modeled as an Eulerian subphase, with mass loss or gain dictating the contraction or expansion of each solid subphase.

(4) Gases produced within the particles are assumed to be immediately released into the gas phase, creating an instantaneous outflow effect. This assumption may overlook the potential delay due to diffusion or other transport mechanisms within the particle. However, in the scope of this work, this simplification helps in focusing on larger-scale phenomena such as overall emissions and temperature profiles.

(5) Emissions from the solid phase enter the gas phase at the same temperature as the solid's outermost layer. When dealing with a heterogeneous mixture of solid wastes,

https://doi.org/10.1021/acsomega.4c07041
ACS Omega 2024, 9, 42010−42026

Table 1. Governing Equations for the Gas Phase and Solid Subphases of the Fuel Bed Model

governing equations	phase	expression
mass conservation	gas	$\frac{\partial}{\partial t}(\varepsilon\rho_g) + \frac{\partial}{\partial x_j}(\varepsilon\rho_g u_{j,g}) = -\sum_N \sum_k S_k^M$ (1)
	solid	$\frac{\partial}{\partial t}[(1-\varepsilon)\alpha_k\rho_k] + \frac{\partial}{\partial x_j}[(1-\varepsilon)\alpha_k\rho_k u_{j,s}] = D_s\frac{\partial^2}{\partial x_j^2}[(1-\varepsilon)\alpha_k\rho_k] + S_k^M$ (2)
momentum conservation	gas	$\frac{\partial}{\partial t}(\varepsilon\rho_g u_{i,g}) + \frac{\partial}{\partial x_j}\left[\varepsilon\rho_g u_{i,g}u_{j,g} - \mu\left(\frac{\partial u_{i,g}}{\partial x_j}\right)\right] = S_{i,M} + S_i(U_{i,g})$ (3)
energy conservation	gas	$\frac{\partial}{\partial t}(\varepsilon\rho_g \bar{c}_{p,g}T_g) + \frac{\partial}{\partial x_j}(\varepsilon\rho_g \bar{c}_{p,g}u_{j,g}T_g) = \frac{\partial}{\partial x_j}\left(\lambda_{eff,g}\frac{\partial T_g}{\partial x_j}\right) + S_{rxn,g} + S_{s-g}$ (4) in which $S_{rxn,g}$ is the heat of gas-phase reactions, and S_{s-g} is the convective heat transfer between gas and solid phase
	solid	$\frac{\partial}{\partial t}[(1-\varepsilon)\alpha_k\rho_k \bar{c}_{p,s}T_k] + \frac{\partial}{\partial x_j}[(1-\varepsilon)\alpha_k\rho_k \bar{c}_{p,s}u_{j,s}T_k] = S_k^E$ (5)
species conservation	gas	$\frac{\partial}{\partial t}(\varepsilon\rho_g Y_{i,g}) + \frac{\partial}{\partial x_j}(\varepsilon\rho_g u_{j,g}Y_{i,g}) = \frac{\partial}{\partial x_j}\left(\rho_g D_{g,eff}\frac{\partial Y_{i,g}}{\partial x_j}\right) + M_{i,g} + M_{i,s}$ (6) in which $M_{i,g}$ is the source of species i from gas reactions, and $M_{i,s}$ is the source of species i from solid reactions

this assumption helps to substantially reduce the complexity of thermal calculations.

2.2. Governing Equations. The fundamental equations governing the fuel bed model include mass, momentum, energy, and species conservation for both gas phase and solid subphases, as outlined in Table 1. To model the thermally thick nature of fuel particles, subgrid models are established. A brief introduction to these subgrid models is provided here, and more details of the source terms in the conservation equations and their application to the Multiple Thermally Thick Particle (MTTP) model can be found in our previous work.[19,20]

Within the mass conservation equations, the source terms for the kth solid subphase, S_k^M, are determined by the reaction kinetics of that subphase and its interactions with adjacent subphases. The energy conservation equations include source terms for the kth solid subphase, S_k^E, comprising five distinct sources that account for changes in sensible enthalpy due to heat transfer and solid-phase reactions.

$$S_k^E = S_{Reac,k} + S_{Cond,k} + S_{blowing,k} + S_{Env,k} + S_{evolution,k} \quad (7)$$

First of all, $S_{Reac,k}$ represents the enthalpy change from chemical reactions and phase changes within the kth subphase

$$S_{Reac,k} = R_k \cdot \Delta H_k \quad (8)$$

$S_{Cond,k}$ accounts for conductive heat transfer across subphases according to Fourier's law.

$$S_{Cond,k} = A_k K_{s,k}\frac{T_{k+1} - T_k}{R_{k+1} - R_k} - A_{k-1}K_{s,k-1}\frac{T_k - T_{k-1}}{R_k - R_{k-1}} \quad (9)$$

$S_{blowing,k}$ addresses the enthalpy shift from gas flow through layers at varying temperatures.

$$S_{blowing,k} = \sum_j^{N_{gas}}\left(\omega_{j,k}^g \int_{T_{ref}}^{T_{k-1}} Cp_j\, dT - \omega_{j,k+1}^g \int_{T_{ref}}^{T_k} Cp_j\, dT\right) \quad (10)$$

$S_{Env,k}$ captures heat transfer in the environment, including convection and radiation.

$$S_{Env,k} = Q_{rad}\cdot\frac{\alpha_N}{\alpha_s} + A_k h_s(T_g - T_k) \quad (11)$$

Finally, $S_{evolution,k}$ denotes the enthalpy variation due to mass transfer in and out of the kth subphase.

$$S_{evolution,k} = \omega_k^s Cp_{s,k}\cdot(T_{k-1} - T_{ref}) - \omega_{k+1}^s Cp_{s,k+1}\cdot(T_k - T_{ref}) \quad (12)$$

The requisite physical and transport properties for these equations are detailed in Table 2.

This study assumes that the shrinkage of fuel particles and the fuel bed is linked to mass loss from each solid subphase. The velocity of the solid phase in the direction parallel to bed height (y-direction) can be determined from the integral expression:

Table 2. Physical and Transport Properties Used in the Fuel Bed Model

parameter	expressions or values
bed porosity	0.40
thermal conductivity (W/(m·K))	$k_{water} = 0.58$ $k_{dry} = 0.13 + 0.0003(T_s - 273)$ $k_{char} = 0.08 - 0.0001(T_s - 273)$ $k_g = \varepsilon(k_f + h_{rv}\Delta l) + \frac{(1-\varepsilon)\Delta l}{\frac{1}{\frac{k_f}{l_v} + h_{rs}} + \frac{l_s}{k_s}}$
convective heat transfer coefficient (W/(m²·K))	$k_{g,eff} = k_g + 0.5Pr\cdot k_g\cdot Re$ $h_{s-g} = k_g\cdot Nu/d_{p,eff}$ $Nu = 2 + 1.1Pr^{1/3}\, Re^{0.6}$
radiation adsorption coefficient	$\kappa = -\frac{1}{d_{p,eff}}\ln\varepsilon$
radiation emissivity	$\epsilon = 0.80$
heat capacity (kJ/(kg·K))	$c_{p,dry\ fuel} = 1.5 + 0.001 \times T$ $c_{p,char} = 0.44 + 0.001 \times T - 7 \times 10^{-8}T^2$ $c_{p,water} = 4.18$ $c_{p,g} = \sum c_{p,i}Y_{g,i}$
gas diffusion coefficient	$D_{g,i} = D_g + 0.5d_p u$
solid diffusion coefficient (cm²/min)	$D_s = 82.2$

https://doi.org/10.1021/acsomega.4c07041
ACS Omega 2024, 9, 42010−42026

Table 3. Rate Expressions and Kinetic Data of Reactions,[6,23] where the General Expression of Kinetic Constants is $k = A\exp(-E/RT)$

rate expressions		A (s^{-1})	E (J/kmol)
$R_{\text{drying},N} = \begin{cases} A_s h_s (C_{w,s} - C_{w,g}) & \text{if } T_{dry} < 373\ \text{K} \\ Q_{cr,N}/H_{evap} & \text{if } T\_\text{dry} \geq 373\ \text{K} \end{cases}$		–	–
$R_{py,N} = k_{py}\rho_{dry}$		1.4×10^{10}	1.50×10^{8}
$R^{j}_{char} = \frac{P_j S_{a,char}}{1/k_j + 1/k_g + 1/k_{ash}}$	$j = O_2$	1.715	8.56×10^{7}
$k_g = \frac{5.06 \times 10^{-7}}{d_p} \times \left(\frac{T_s + T_g}{2}\right)^{0.75}$ and $k_{ash} = L_{ash}/D_{ash}$	$j = CO_2$	3.42	1.48×10^{8}
	$j = H_2O$	3.42	1.10×10^{8}
$H_2 + \frac{1}{2}O_2 \xrightarrow{R_{g,1}} H_2O$, $R_{g,1} = k_{g,1}C_{H_2}C_{O_2}$		1.0×10^{11}	4.1987×10^{7}
$CH_4 + \frac{3}{2}O_2 \xrightarrow{R_{g,2}} 2H_2O + CO$, $R_{g,2} = k_{g,2}C^{0.5}_{CH_4}C_{O_2}$		5.012×10^{11}	2.0×10^{8}
$CH_4 + H_2O \xrightarrow{R_{g,3}} 3H_2 + CO$, $R_{g,3} = k_{g,3}C_{CH_4}C_{H_2O}$		3.0×10^{8}	1.256×10^{8}
$CO + \frac{1}{2}O_2 \xrightarrow{R_{g,4}} CO_2$, $R_{g,4} = k_{g,4}C_{CO}C^{0.25}_{O_2}C^{0.5}_{H_2O}$		2.32×10^{12}	1.67×10^{8}
$CO + H_2O \xrightarrow{R_{g,5}} CO_2 + H_2$, $R_{g,5} = k_{g,5}C_{CO}C_{H_2O}$		2.78	1.26×10^{7}
primary tar $\xrightarrow{R_{g,6}}$ CO + CO_2 + CH_4 + H_2 + H_2O, $R_{g,6} = k_{g,5}C_{\text{primary tar}}$		4.28×10^{6}	1.08×10^{8}
$NH_3 + O_2 \xrightarrow{R_{N,1}} NO + \cdots$, $R_{N,1} = k_{N,1}C_{NH_3}C_{O_2}/(C_{O_2} + 0.054)$		6.75×10^{6}	$1.00 \times 10^{4} \times R$
$HCN + O_2 \xrightarrow{R_{N,2}} NO + \cdots$, $R_{N,2} = \frac{k_{N,2}C_{HCN}C_{O_2}}{1 + 1.02 \times 10^{9}\exp\left(-\frac{25460}{T}\right)C_{NO}}$		2.40×10^{5}	$1.00 \times 10^{4} \times R$
$NH_3 + NO \xrightarrow{R_{N,3}} N_2 + \cdots$, $R_{N,3} = k_{N,3}C^{0.29}_{NH_3}C^{0.64}_{NO}$		8.20×10^{4}	$1.20 \times 10^{4} \times R$
$HCN + NO \xrightarrow{R_{N,4}} N_2 + \cdots$, $R_{N,4} = k_{N,4}C_{HCN}C_{O_2}$		2.25×10^{4}	$1.20 \times 10^{4} \times R$
$[C - N] + O_2 \xrightarrow{R_{N,5}} NO + N_2$, $R_{N,5} = 0.50 \times R^{O_2}_{char} \times N/C$, N and C refer to the molar ratio of nitrogen and carbon in char		–	–
$C(s) + NO \xrightarrow{R_{N,6}} N_2 + CO$, $R_{N,6} = k_{N,6}C^{0.7}_{NO}$		2.06×10^{5}	16,180 × R

$$u_{y,s} = -\frac{1}{1-\varepsilon}\int_0^y \sum_N (R_{\text{drying},N}\theta_{\text{drying},N} + R_{\text{devol},N}\theta_{\text{devol},N} + R_{\text{char},N}\theta_{\text{char},N})\mathrm{d}y \quad (13)$$

in which $\theta_{\text{drying},N}$, $\theta_{\text{devol},N}$, and $\theta_{\text{char},N}$ are the shrinkage coefficients due to drying, devolatilization, and char reactions, respectively.

In addition, the fuel bed experiences not only a downward movement due to shrinkage but also random mixing resulting from the action of the grate, commonly a reciprocating type. This mixing effect is modeled after the studies by Yang et al.[21] and Nakamura.[22] The mixing is conceptualized as a diffusion process, drawing parallels between the stochastic motion of fuel particles and the molecular diffusion in gases. Consequently, Fick's law is employed to derive the diffusion component in the mass conservation equations for the solid subphases. The diffusion coefficient is assigned a value of 82.2 cm^2/min, in line with the recommendation by Yang et al.[21]

2.3. Reaction Models. The modeling of reactions in the fuel bed is divided into three primary segments: (1) solid phase transformations, which include processes such as drying, devolatilization, and heterogeneous char conversions, (2) combustion of volatile gases produced during devolatilization, and (3) NO_x formation and reduction reactions, which encompass the oxidation of nitrogenous precursors (NH_3 and HCN) as well as the reduction of NO_x through both homogeneous and heterogeneous processes. The corresponding rate formulas and kinetic parameters are listed in Table 3.

To compute the drying rates of fuel particles, an approach that merges an equilibrium model with a thermal model is used. Gómez et al.[24] have provided a detailed methodology for assessing the thermally driven drying rates for particles that are thermally thick. Devolatilization is represented by a single, overarching reaction, with kinetic parameters derived from Lin et al.[25] The devolatilization products include a range of light gases, a combined tar fraction, NO_x precursors, and char. The distribution of these products and the computation of the primary tar are based on an approach that ensures the balance of elements and the conservation of the heating value. Ngamsidhiphongsa et al.[26] have outlined the detailed process for these computations.

Gas-phase reactions are modeled to account for turbulent flow by utilizing both finite-rate and eddy-dissipation models to calculate reaction rates. The effective reaction rate is determined by taking the lesser value of the two:

$$R_{g,i} = \min(R_{\text{kin},i}, R_{\text{eddy},i}) \quad (14)$$

Where $R_{\text{kin},i}$ is the rate of the chemical reaction and $R_{\text{eddy},i}$ is the eddy-dissipation rate. The finite-rate kinetic calculations rely on the Arrhenius equation, while the eddy-dissipation rate is influenced by the large-eddy mixing time scale:

$$R_{\text{eddy},i} = 0.63\frac{\rho}{\bar{W}}\left(\frac{1.75(1-\varepsilon)V}{\varepsilon d_p}\right)\min\left(\frac{y_i}{\nu_{i,j}}\right) \quad (15)$$

The fate of nitrogen in the fuel (fuel-N) significantly affects NO_x emissions and is dependent on the fuel's characteristics

https://doi.org/10.1021/acsomega.4c07041
ACS Omega 2024, 9, 42010−42026

and operational conditions. The following assumptions simplify nitrogen chemistry while capturing the key steps of nitrogen conversion:

(1) The partitioning of fuel-N into volatile-N and char-N is based on the ratio of volatile to fixed carbon, obtained by the proximate analysis of the solid fuel.[27]
(2) Volatile-N is predominantly released as NH_3 and as nitrogen in primary tar, with HCN being released upon the breakdown of primary tar.[28] An NH_3 to HCN ratio of 80:20 is assumed, reflecting the findings that NH_3 is the more prevalent nitrogenous species.[29]
(3) The oxidation of nitrogenous precursors is considered to produce only NO, disregarding the formation of N_2O and other nitrogen compounds. Similarly, the reduction of NO is expected to yield only N_2.
(4) The oxidation of char-N is correlated with the consumption of carbon in the char, with an estimated 50% of char-N being converted to NO, following the findings of Ulusoy et al.[30]

Based on these assumptions, the NO_x conversion reactions within the fuel bed ($R_{N,1} - R_{N,6}$) are also given in Table 3.

3. DESCRIPTION OF THE MSW INCINERATOR

3.1. Incinerator Configurations and Fuel Properties. The middle-arch MSW incinerator studied in this work has an MSW disposal capacity of 500 tons/day, and its schematic diagram is given in Figure 1.

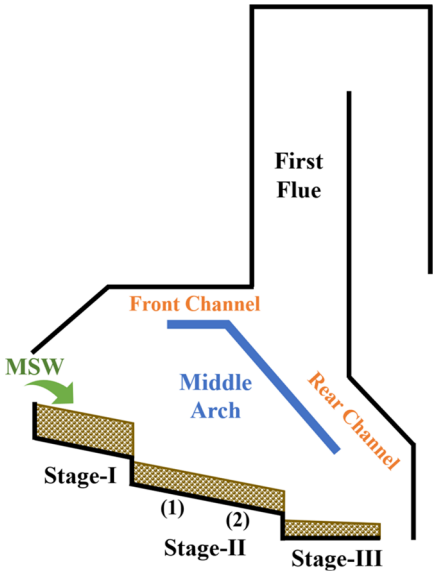

Figure 1. Schematic diagram of the middle-arch MSW incinerator.

The middle arch is its feature structure, by which the direct path from the bed to the first flue is blocked, forming two gas flow channels with the front and rear arch separately. The gases from the two channels are designed to mix and react at the bottom of the first flue, which theoretically would lead to a complete gas-phase combustion and a low NO_x emission. The combustion process of the MSW bed is divided into three stages. The first and second stages of the grate are designed with a tilt, while the third stage of the grate is designed horizontally to ensure complete combustion of the solid phase. Generally, the combustion process mainly occurs on the stage-II grate, which has two separate air chambers, while stage-I and stage-III each have one air chamber.

The quality of MSW processed by the incinerator fluctuates daily, and representative data is used in the present study, as shown in Table 4. Due to the implementation of waste classification policies, there is a significant reduction in the moisture content of the MSW, which leads to a lower heating value (LHV) of 11.635 MJ/kg. Ultimate and proximate analyses are also given in Table 4.

Table 4. Fuel Properties of MSW

properties	value (wt %)
proximate analysis (ar)	
moisture (M)	38.00
volatile (V)	39.96
fixed carbon (FC)	6.67
ash (A)	15.37
lower heating value (LHV, MJ/kg)	11.635
ultimate analysis (daf)	
C	55.36
H	11.32
O	31.57
N	1.75
S	not detected

3.2. Settings for Numerical Modeling. During grid generation, the MSW incinerator was segmented using a structured grid approach, and regions experiencing substantial fluctuations in turbulence, such as the adjacent grate area and the throat region where the secondary air (SA) inlet is located, underwent grid refinement for better accuracy. To verify that the simulation results were not affected by the size of the grid used, a series of initial simulations were conducted with varying numbers of cells: 752,633; 1,839,248; 2,533,947; 3,311,531; and 5,728,145. Analysis of the simulation data indicated that temperature variations were less than 0.1% when comparing the results from grids containing 3,311,531 cells to those with 5,728,145 cells. This outcome suggested that a grid comprising 3,311,531 cells had the necessary precision for accurate simulation outcomes. Within the freeboard area of the boiler, the finite-rate/eddy-dissipation concept was applied to model homogeneous chemical reactions, while the standard $k-\varepsilon$ model was selected for simulating the turbulent hydrodynamic behavior. For the prediction of radiative heat transfer, the P-1 radiation model was used. To properly account for the impact of gas emissivity on radiative heat transfer, a critical aspect, the weighted-sum-of-gray-gases model (WSGGM) was adopted for a more realistic representation.

The specific configurations used in the simulations are listed in Table 5. Detailed explanation for these configurations will be given in the subsequent Section 4, and only a brief introduction will be given here. In case 1, configrations in the calculations were set referring to the common operation condition of the MSW incinerator. In case 2, the total amount of primary air (PA) was reduced, while the secondary air (SA) was correspondingly increased. In case 3, further adjustments were implemented in both the primary air distribution and the grate velocity.

https://doi.org/10.1021/acsomega.4c07041
ACS Omega 2024, 9, 42010−42026

Table 5. Specific Configurations Used in the Simulations

	configurations			
case 1	**PA distribution** (kg·m^2/s)			
	stage-I: 0.1002	stage-II (1): 0.3533	stage-II (2): 0.3533	stage-III: 0.0618
	SA distribution (kg/s)			
	side wall-middle: 0.45 × 4	side wall-rear: 0.38 × 2	rear arch: 1.05	
	grate velocity (m/s)			
	stage-I: 0.0028	stage-II (1): 0.0022	stage-II (2): 0.0022	stage-III: 0.0024
case 2	**PA distribution** (kg·m^2/s)			
	stage-I: 0.0802	stage-II (1): 0.2827	stage-II (2): 0.2827	stage-III: 0.0495
	SA distribution (kg/s)			
	side wall-middle: 0.65 × 4	side wall-rear: 0.65 × 2	rear arch: 1.85	
	grate velocity (m/s)			
	stage-I: 0.0028	stage-II (1): 0.0022	stage-II (2): 0.0022	stage-III: 0.0024
case 3	**PA distribution** (kg·m^2/s)			
	stage-I: 0.0822	stage-II (1): 0.1976	stage-II (2): 0.1976	stage-III: 0.1728
	SA distribution (kg/s)			
	side wall-middle: 0.65 × 4	side wall-rear: 0.65 × 2	rear arch: 1.85	
	grate velocity (m/s)			
	stage-I: 0.0022	stage-II (1): 0.0018	stage-II (2): 0.0018	stage-III: 0.0016

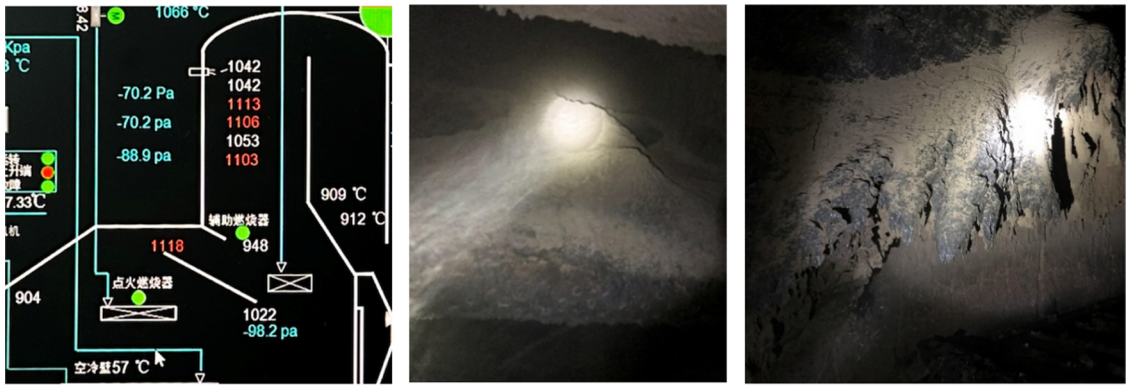

(a) Local overheating (b) Slagging at front channel (c) Slagging below middle arch

Figure 2. Photos of the typical state of the incinerator under common operation conditions.

4. RESULTS AND DISCUSSION

4.1. Common Conditions of the Incinerator. The common operation conditions of the incinerator are presented as case 1 in Table 5, with primary air serving as the main O_2 source and secondary air serving as a supplement. The ratio of the total flow rate of the primary air to the secondary air was approximately 8:2. During common operation, issues such as high-temperature slagging and high original NO_x emission concentration were encountered. The original NO_x emission concentration refers to the concentration from the combustion process, with no NO_x control measure such as SNCR, PNCR, or SCR. The typical state of the incinerator is illustrated in Figure 2.

The temperature distribution within the furnace, as shown in Figure 2a, indicates that the horizontal front channel formed by the front and middle arches exhibits a locally high temperature of up to 1118 °C, predisposing this area to high-temperature slagging. Not unexpectedly, the slagging problem is found to almost block the horizontal front channel, as shown in Figure 2b, which adversely affects gas flow and combustion organization within the furnace, necessitating frequent shutdowns for deslagging operations. Figure 2a also revealed that the vertical first flue also exhibits an issue of excessive temperatures. Additionally, a serious slagging problem is found below the middle arch, as shown in Figure 2c. The absence of thermocouples in this area precludes the observation of the temperature distribution.

Aside from these localized overheating issues, the operation mode also results in a high NO_x emission. Despite the deployment of NO_x control measures such as SNCR, PNCR, and SCR on-site, NO_x emission concentration still fluctuates within the range of 100−200 mg/(N·m^3). To meet environmental regulations, sometimes the load must be restricted to inhibit NO_x formation. The high NO_x emission hugely increases the consumption of NO_x control reagents and catalysts, leading to higher operating costs for the incinerator.

In order to reveal the causes of local overheating and high NO_x emissions, a numerical simulation of the combustion process, including both the bed combustion on the grate and the gas-phase freeboard combustion in the furnace, was carried out using the established CFD model. The bed combustion state is given in Figure 3, while the freeboard combustion is depicted in Figure 4. The temperature distribution in the bed, as shown in Figure 3a, indicates that combustion does not occur in most of the area of the first stage of the grate, and ignition is only observed at the top surface of the bed near the end of this stage. Therefore, a large proportion of O_2 enters the bed from bottom, goes through the bed unreacted, and directly

https://doi.org/10.1021/acsomega.4c07041
ACS Omega 2024, 9, 42010−42026

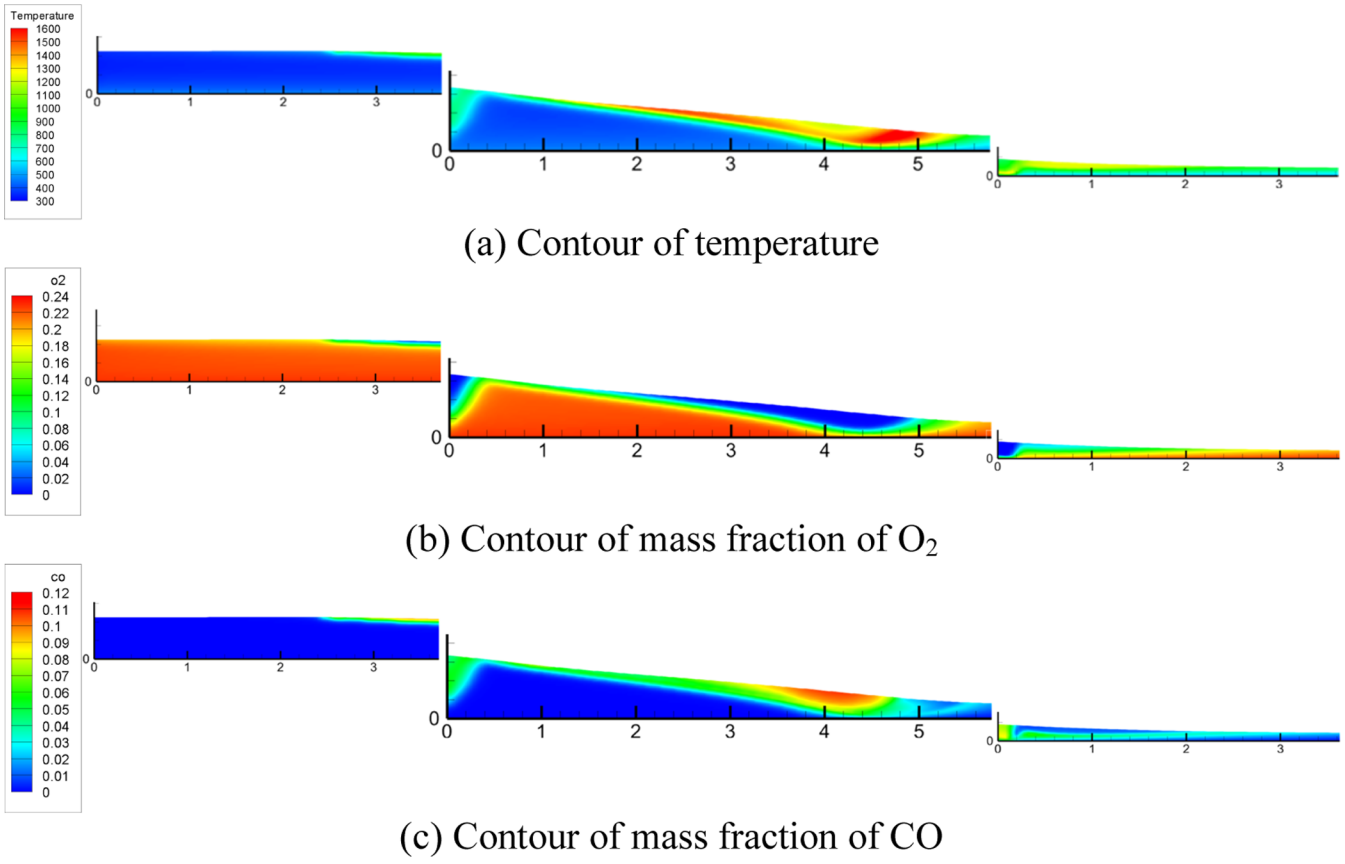

Figure 3. Bed combustion state under common operation conditions.

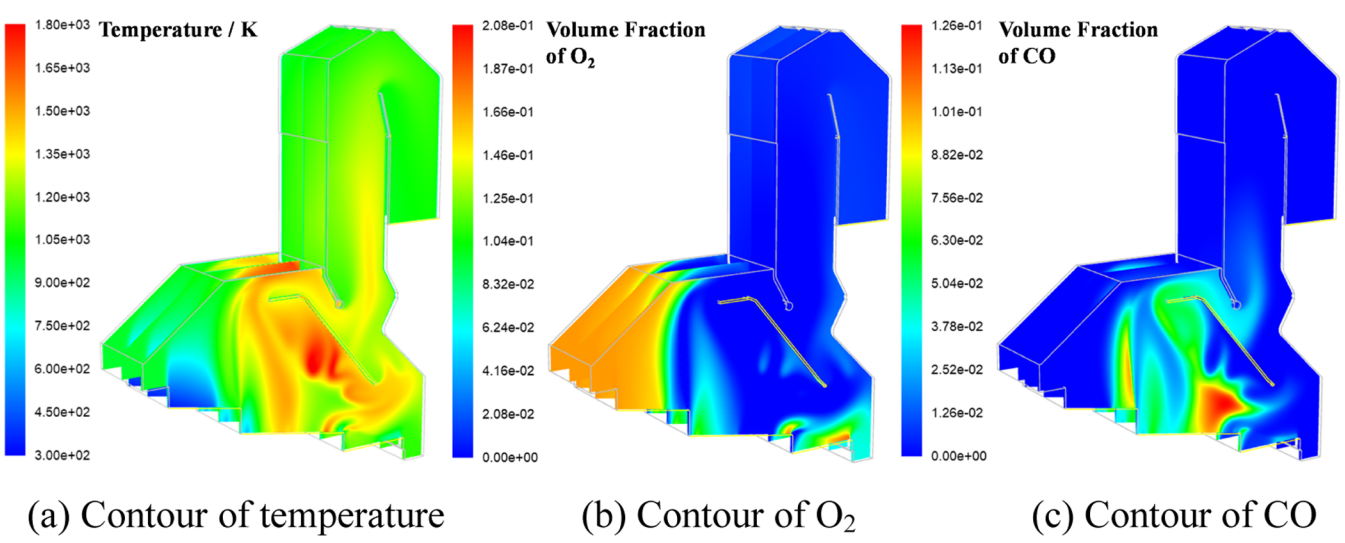

Figure 4. Freeboard combustion state under common operation conditions.

enters the freeboard, as shown in Figure 3b. Only near the end of the first stage, a small portion of O_2 is consumed and generates CO, see Figure 3c. The second stage of the grate is where bed combustion mainly occurs. The temperature distribution in this stage clearly shows the propagation of combustion from the top surface of the bed downward to the bottom. Regarding the distribution of gas components in the second stage, almost all the O_2 entering the bed is consumed during the flame propagation region, and products released at the top surface of this region are primarily combustible gases such as CO. As for the third stage of the grate, burnout of char is the main reaction, which is enhanced in the front of the stage due to the step-fall effect, consuming a portion of O_2 and generating some combustible gases.

As for the gas-phase combustion in the freeboard, the temperature distribution in Figure 4a confirms the existence of a localized high temperature within the horizontal front channel formed by the front and middle arches, which is the main cause of slagging blockage at this location. Analyzing the distribution of O_2 and CO in Figure 4b,c, consistent with the

https://doi.org/10.1021/acsomega.4c07041
ACS Omega 2024, 9, 42010−42026

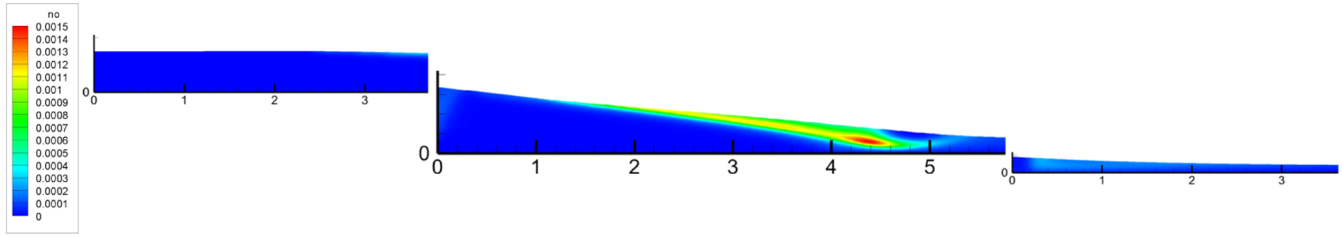

(a) Contour of mass fraction of NO

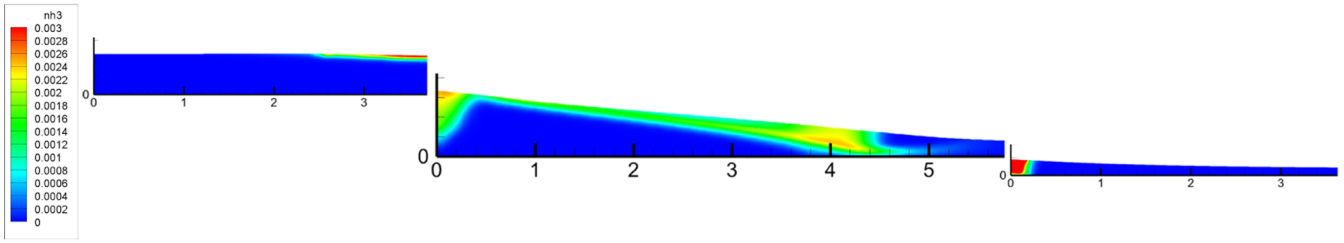

(a) Contour of mass fraction of NH_3

Figure 5. Distribution NO and NH_3 in bed under common operation conditions.

product distribution at the bed surface, a large amount of O_2 passes through the unignited region of the first stage and flows upward along the front arch. In the second stage, volatiles are released intensively, generating a significant amount of CO and other combustible gases. Guided by the front and middle arches, O_2 and combustible gases mix at the entrance to the horizontal front channel and combust within the channel, leading to a localized high temperature.

Additionally, a region of high temperature below the middle arch is also found, which is the cause of severe slagging shown in Figure 2c. The formation of localized high temperatures in this region mainly stems from the concentrated release of combustible gases, such as CO, from the second stage of the bed. As Figure 4c illustrates, these combustible gases rise and encounter secondary air injected from the sidewalls, leading to strong combustion and a high temperature.

The high temperatures measured in the vertical first flue may result from an uneven temperature distribution due to gas-phase combustion. CO distribution given in Figure 4c reveals that the concentrated CO released from the bed does not completely combust in the horizontal front channel, but instead enters the vertical first flue to undergo gas-phase combustion reactions. Correspondingly, the temperature distribution shown in Figure 4a demonstrates that the area of CO combustion occurs within the first flue and creates localized high temperature near the rear wall, leading to an uneven overall temperature distribution in the flue.

After clarifying the mechanism of localized high-temperature generation in the furnace under common operation conditions, further analysis on the formation and reduction of NO_x will be conducted, from the release from the bed to the conversion in the freeboard. Figure 5 presents the distribution of NO and NH_3 during the combustion process. It can be noticed that the formation of NO mainly happens at the flame front. As it flows upward through the bed, it undergoes reduction reactions with NH_3 and char, leading to a decrease in the concentration. The generation of NH_3 precedes NO, starts with the ignition of the bed, and is released in large quantity during the pyrolysis of MSW. As NH_3 flows upward through the bed, a portion of it is oxidized to NO, while another portion reacts with NO and converts to N_2.

To more clearly present the effects of the amount and speciation of N released from the bed on the formation and reduction of NO in the freeboard, the distributions of NO and NH_3 at the top surface of the bed are given in Figure 6. It is

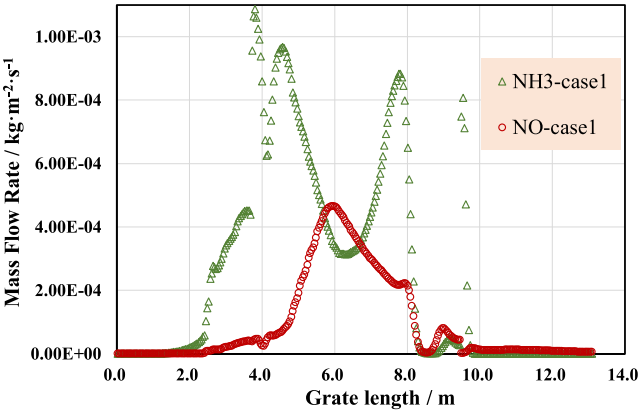

Figure 6. Distributions of NO and NH_3 released from the bed under common operation conditions.

apparent that, in terms of quantity, the NH_3 at the top surface of the bed far exceeds NO, and its highest mass flow rate exceeds 1.00×10^{-3} kg/(m^2·s) while the peak of NO is below 0.50×10^{-3} kg/(m^2·s). Theoretically, NH_3 entering the freeboard should be enough to convert all of the NO into N_2. However, it is important to note that products released from the bed greatly changed in different regions along the direction of grate movement, referring to the different status of bed combustion. At a position approximately 6.0 m from the MSW entrance, NO formation reaches its peak, while the amount of NH_3 is lower than NO. Additionally, in the third stage of the grate, char-N is also converted into NO during the char burnout process, but by then almost no NH_3 is produced. Therefore, these two regions will be the main NO-rich zones in subsequent freeboard combustion.

https://doi.org/10.1021/acsomega.4c07041
ACS Omega 2024, 9, 42010−42026

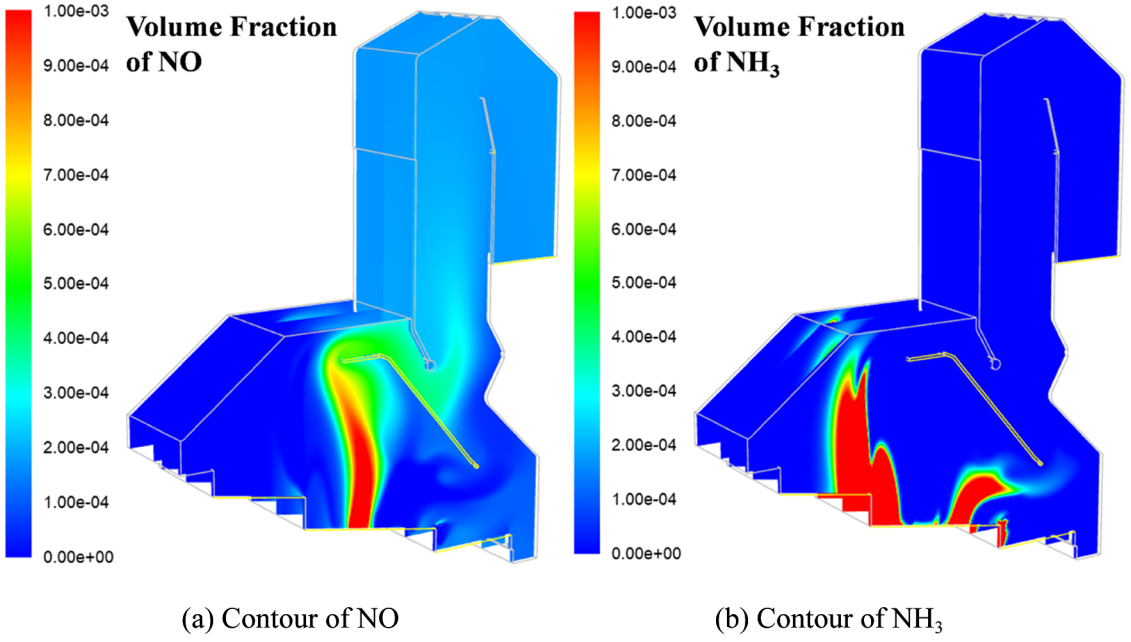

Figure 7. Distribution of NO and NH_3 in freeboard under common operation conditions.

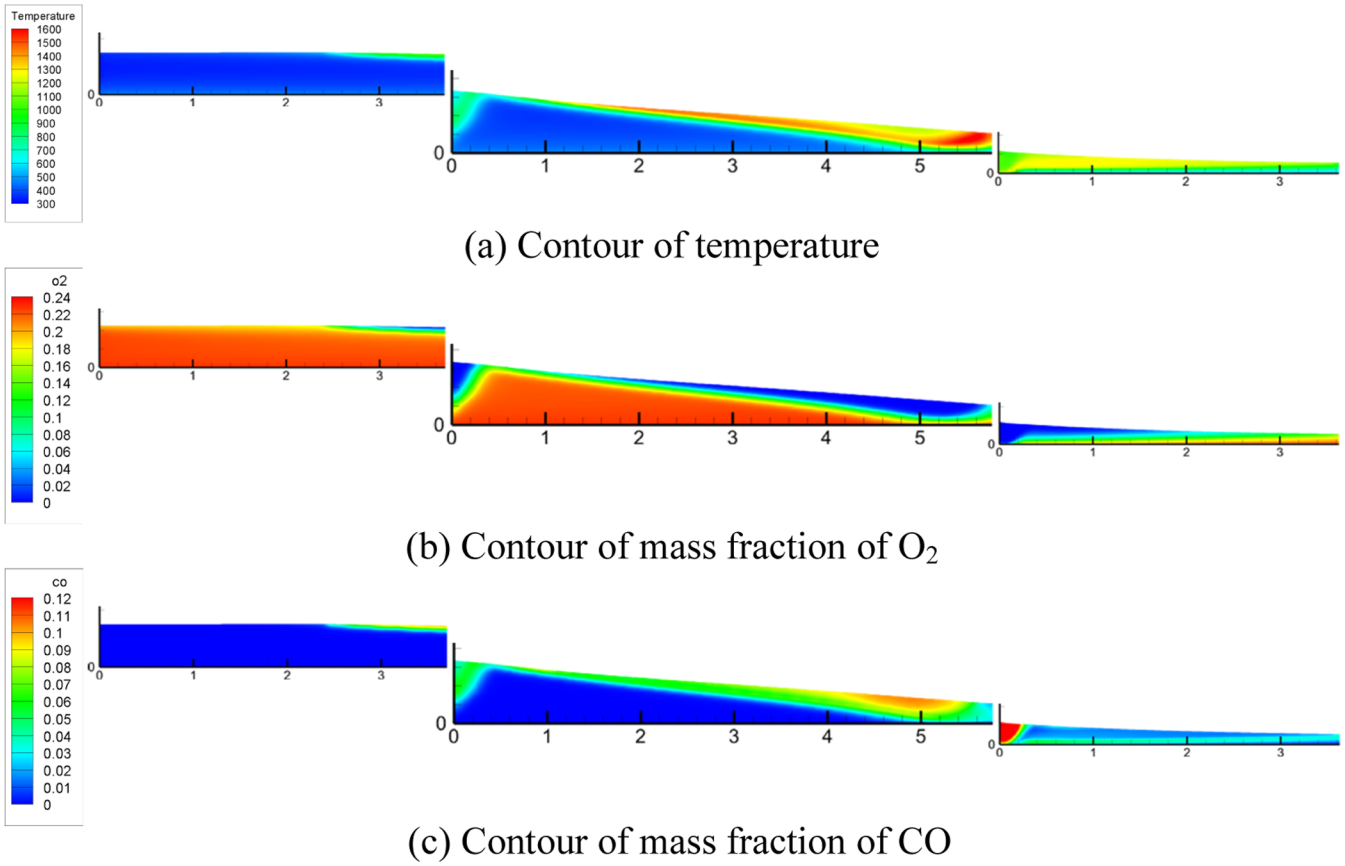

Figure 8. Bed combustion state with primary air reduced.

For freeboard combustion, distributions of NO and NH_3 are given in Figure 7. Consistent with the discussion above, a concentrated NO flow can be observed at the 6.0 m position of the grate, and a smaller amount of NO released from the third stage can also be observed. NH_3 is released next to the concentrated NO flow on both sides. NO flows upward, entering the vertical first flue through the horizontal front channel. While NH_3 is gradually oxidized and consumed during its ascent, and does not sufficiently mix and react with NO. The modeling result indicates that even with the oxygen volume fraction at the boiler outlet as low as 2.72%, which should theoretically facilitate NO reduction, the original

https://doi.org/10.1021/acsomega.4c07041
ACS Omega 2024, 9, 42010−42026

emission concentration of NO_x remains high at 243.55 mg/(N·m^3). The NO_x emission level is consistent with the actual situation on site considering the control measures deployed.

Based on the numerical simulation analysis of the combustion status of the incinerator under common operation conditions, the main cause of the local overheating issue in the horizontal front channel is the concentrated combustion of combustible gases such as CO in it, which is a comprehensive outcome of three factors. First, a large amount of primary air leads to the concentrated release of volatiles from the second stage of the bed. Second, a smaller amount of secondary air is hard to ensure a complete combustion of the volatiles released from the bed, in the spacious area below the middle arch. Lastly, due to the large primary air, the ignition of the fuel bed on the first stage is delayed, and more unconsumed O_2 passes through the bed layer into the freeboard, which then mixes with CO and other combustible gases near the entrance of the horizontal front channel, under the joint guidance of the front and middle arches.

The reason for the high NO_x emission is essentially similar to the local overheating issue, the concentrated release of NO from the fuel bed directly flowing into the vertical flue through the horizontal front channel without sufficiently mixing and reacting with NH_3, which is also caused by three factors. First, the large primary air causes a concentrated release of NO from the fuel bed in the second stage. Second, the large primary air promotes the oxidation of NH_3, resulting in more nitrogen being released from the bed in the form of NO. Lastly, under large primary air, the combustion of the bed is more concentrated toward the front part of the grate, causing the NO release position to be forward. Then, under the current flow field, almost all NO flows into the horizontal front channel, unable to form the counterflow mixing and reaction between NO and NH_3, which is thought to be created by the middle arch and its two channels.[15]

Through the discussion above, although the mechanisms behind the local overheating and high NO_x emission under common operation conditions are complex, they can be simply attributed to the same macroscopic reason, which is the unreasonable ratio of primary to secondary air. Therefore, in the subsequent optimization, the adjustment of the ratio of primary to secondary air will be first considered, and its impact on the combustion and NO_x emission will be studied.

4.2. Effect of the Ratio of Primary to Secondary Air.

Based on the above discussion, the ratio of primary air is reduced and, correspondingly, the secondary air is increased, while other operating conditions remain unchanged. The specific operating parameters are shown in Table 5 as case 2. Using the established model, numerical simulations are conducted to evaluate and analyze combustion and NO_x emission under this scenario.

First, Figure 8 presents the distributions of temperature, O_2, and CO in the bed after reducing the primary air. It can be seen that drying and ignition of the bed on the first stage of the grating are not significantly affected. However, in the second stage, when the velocity of primary air is in the "oxygen-limited" zone,[31] the reduction in air velocity leads to slower flame propagation, resulting in a significantly longer fire bed. Consequently, under the combined effect of the reduced primary air and the extended fire bed, a higher proportion of the O_2 is consumed by the combustion in the bed, and both the range and the total amount of the O_2 passing through the bed into the freeboard are significantly reduced. Besides, compared with Figure 3c, the extended fire bed causes CO to be generated in a wider range of the bed, eliminating the concentrated emission observed under common operation conditions. In addition, based on the temperature distribution, it can be inferred that the carbon burnout stage is not completed on the second section of the grate, and some unburned carbon falls into the third stage. Under the effect of the drop between stages, it will be more conducive to the burnout of carbon in the bed at the front end of the third stage, which could be proved by the generation of CO observed at the front end of the third stage in Figure 8c.

To quantitatively evaluate the changes in gases released from the bed caused by reducing the primary air, the distribution of the mass flow rate of O_2 and CO at the top surface of the bed before and after the adjustment is compared in Figure 9. After

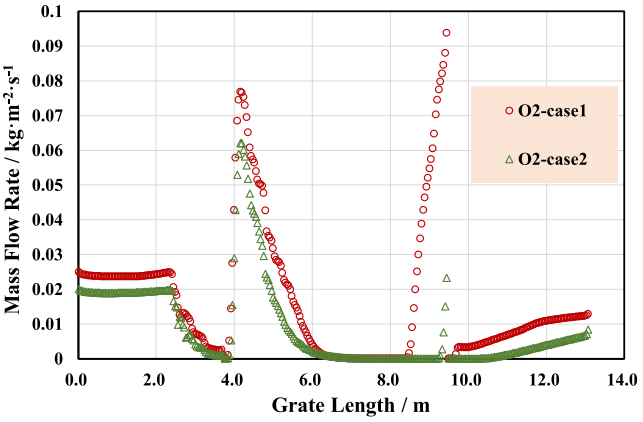

(a) Mass flow rate of O_2 at the top surface of bed

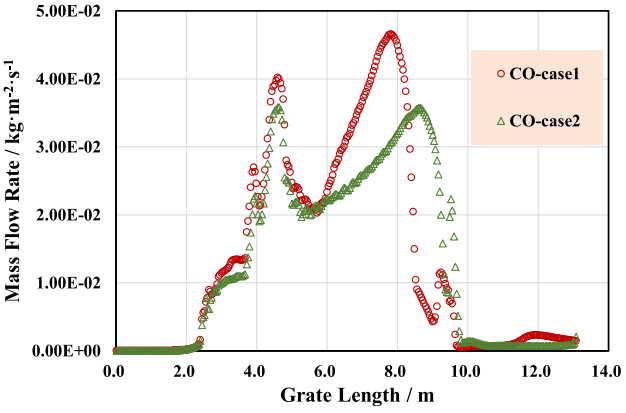

(b) Mass flow rate of CO at the top surface of bed

Figure 9. Distribution of O_2 and CO at the top surface of the bed before and after reducing primary air.

the reduction of primary air, the amounts of aqueous O_2 released from all three stages of the bed are clearly reduced. Especially at the end of the second stage, under common operation conditions, a large amount of O_2 is emitted since the in-bed combustion reaction is finished here; whereas after adjustment, due to the extension of the fire bed, no significant O_2 emission occurs at this position. As for CO, the concentrated emission of CO from the bed under common operation conditions is an important reason for the localized high temperature in the horizontal front channel. After adjusting the primary air, the range of CO emission is broadened, and its peak value decreases from 4.6×10^{-2} to 3.5

https://doi.org/10.1021/acsomega.4c07041
ACS Omega 2024, 9, 42010−42026

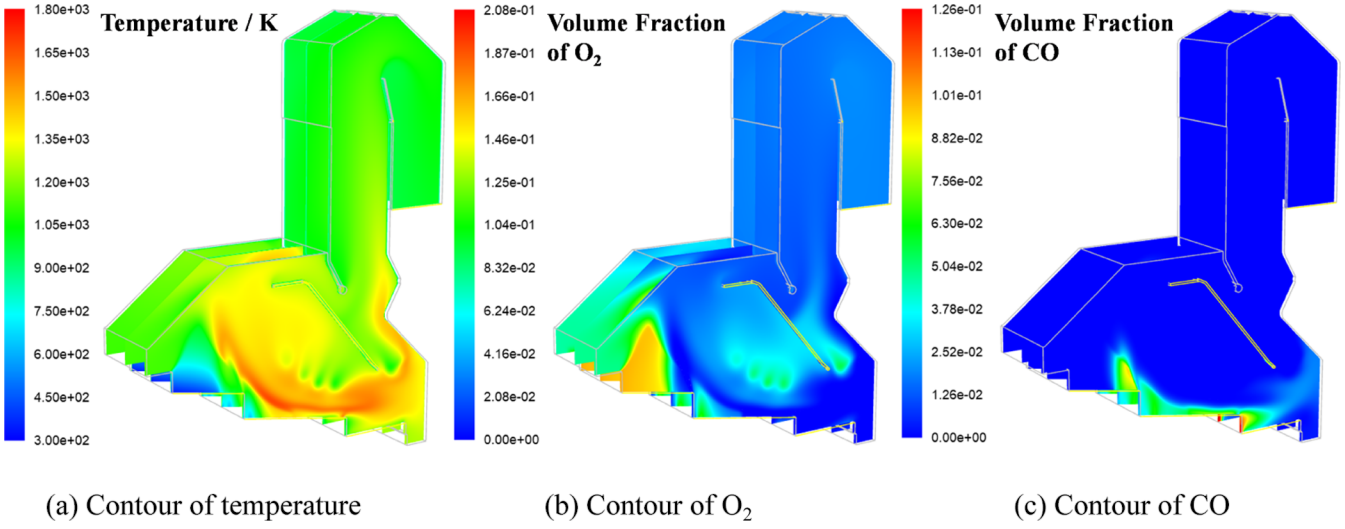

Figure 10. Freeboard combustion state with primary air reduced.

$\times 10^{-2}$ kg/(m^2·s), which helps to solve the local overheating problems in the furnace.

After the improvement of the combustion condition in the fuel bed and the distribution of its products, further analysis is conducted on the gas-phase combustion in the freeboard. Figure 10 shows the temperature and component distribution in the freeboard after adjustment of the ratio of primary to secondary air. In the spacious space below the middle arch, compared to the common operation condition (Figure 4a), the temperature distribution is more uniform. First, this is partly due to the moderate extension of the fire line in the fuel bed, resulting in more uniform distribution of volatiles. Second, the increase in the proportion of secondary air enhances the oxygen supply below the middle arch. Comparing Figures 4b and 10b, more O_2 appears in this area and exceeds the need for the combustion of CO and other volatiles. Third, the larger secondary air jet also enhances the mixing effect of volatiles with O_2. Under the joint effect of these three aspects, the combustion of volatiles below the middle arch is more complete; as shown in Figure 10c, CO is almost completely consumed near the top surface of the bed. Consequently, the temperature near the bed surface gets higher, and its distribution below the middle arch is more uniform. As a result, the issues of localized high temperature below the middle arch and in the horizontal front channel have been significantly improved.

As for the NO_x emission, the release of NO and NH_3 from the bed is also similarly extended, following the layer combustion process. Considering that, under common operation conditions, the concentrated NO flow at 6.0 m on the grate is the main factor contributing to high NO_x emission, changes at this location are carefully observed after adjusting the primary to secondary air ratio, as shown in Figure 11. After reducing primary air, the maximum mass flow rate of NO decreases from 4.6×10^{-4} to 3.8×10^{-4} kg/(m^2·s). Contrarily, the mass flow rate of NH_3 at that position does not show an obvious decrease; instead, there is even a noticeable increase in the later part of the flame propagation process (after 6.3 m). Although the reduction in primary air slowed the in-bed combustion rate, as well as the release of NH_3, it also weakened the oxidation of NH_3. Therefore, at the 6.0 m position where the release of NO reaches its maximum,

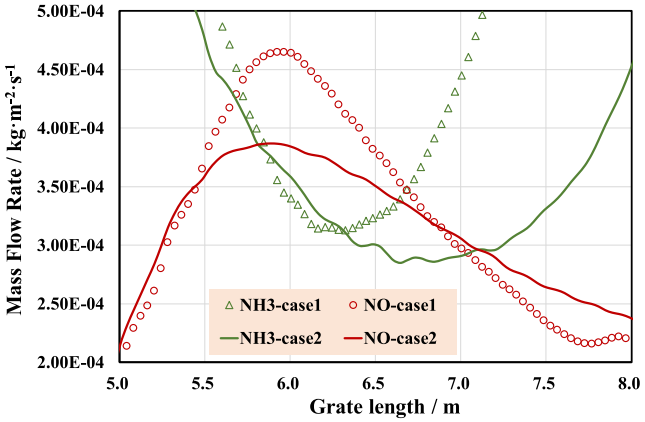

Figure 11. Distribution of NO and NH_3 at the top surface of the bed after reducing primary air.

although the amount of NO is still slightly higher than that of NH_3, the gap between them is significantly reduced compared to the common operation condition (case 1).

Then, the distribution of NO and NH_3 within the freeboard is observed, as shown in Figure 12. It can be found that the "chimney flow" of NO in the freeboard under common operation conditions has disappeared. This is partly due to the aforementioned reduction in the peak value of NO release from the bed, and the increase in secondary air also enhances the mixing and reaction under the middle arch. Also, the enhanced mixing and oxidation reactions lead to the complete consumption of NH_3 at a lower position close to the bed. Some react with NO to reduce it, while the rest is oxidized into NO. Under this condition, the volume fraction of O_2 at the boiler outlet is 3.37%, and the original NO_x emission is reduced from 243.55 to 161.54 mg/(N·m^3).

In summary, the numerical simulation analysis reveals that adjusting the ratio of primary to secondary air extends the combustion process within the fuel bed and leads to a more uniform distribution of products on the bed surface. The gas-phase combustion of volatiles under the middle arch is more complete, and the temperature distribution is more uniform, effectively resolving the local overheating problems in the horizontal front channel and under the middle arch. At the same time, the concentrated release of NO from the bed is

https://doi.org/10.1021/acsomega.4c07041
ACS Omega 2024, 9, 42010−42026

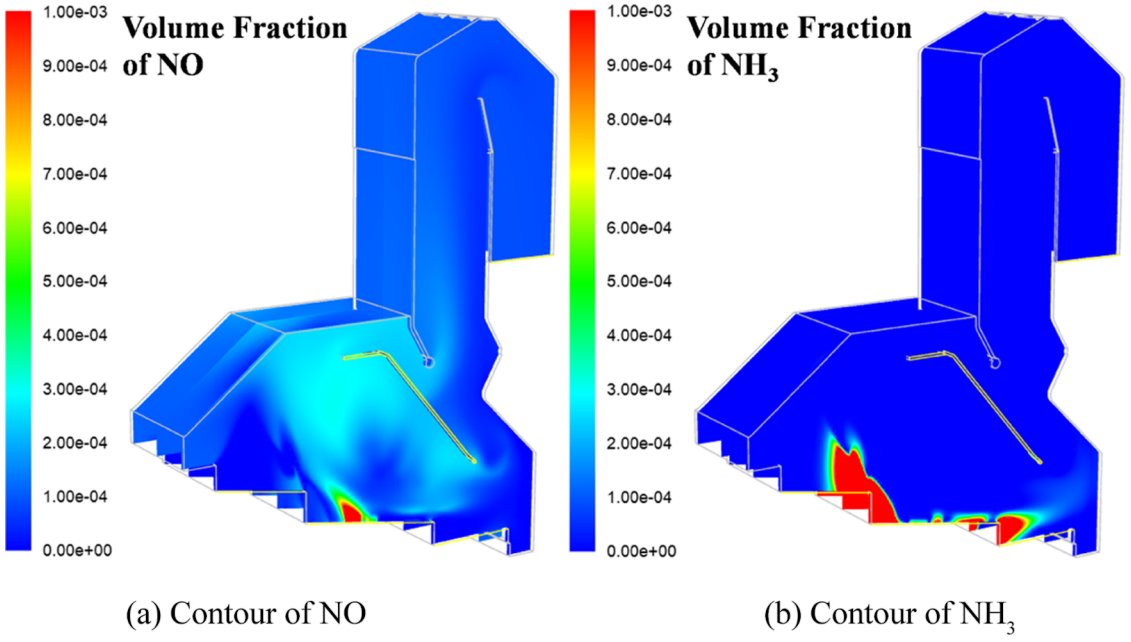

Figure 12. Distribution of NO and NH_3 in freeboard after primary air was reduced.

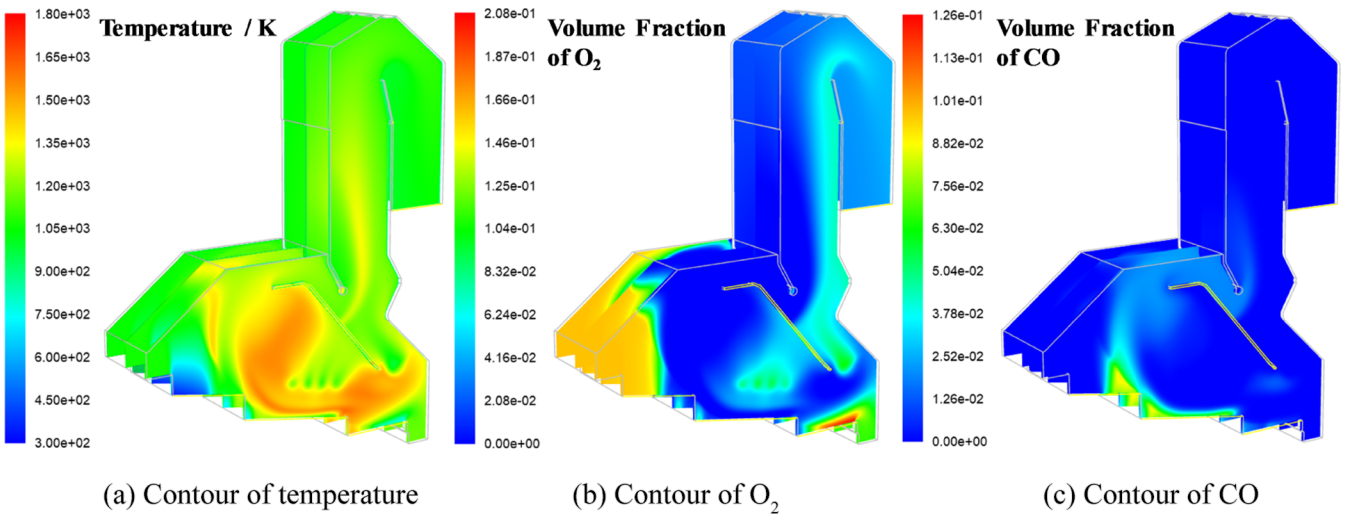

Figure 13. Freeboard combustion state after the primary air distribution was adjusted.

alleviated and the original NO_x emission is appreciably reduced. However, NO still primarily enters the vertical first flue through the horizontal front channel without undergoing the intended counterflow mixing and reduction with NH_3, indicating there is still significant potential for optimization. To adjust the component distribution in front and rear channels, modifying the distribution of products released from the bed is an effective method. Therefore, the following step will further regulate the in-bed combustion process to adjust the product distribution in the two channels, thereby fully utilizing the counterflow mixing and reduction functions of the middle arch.

4.3. Effect of Primary Air Distribution. Based on the above discussion, with the total amount of primary air remaining unchanged, further adjustment is made to the distribution of primary air across different stages, and detailed information is given in Table 5 as case 3. This primarily involves moderately reducing the air flow rate in the second stage and increasing the supply in the third stage. Additionally, the move speeds in the three stages of the grate are reduced by varying degrees, to form a higher bed.

In terms of combustion, Figure 13 displays the distributions of temperature, O_2, and CO in the freeboard after adjustment. As seen in the temperature distribution (Figure 13a), the ignition of the bed is slightly earlier. This change is attributed to the decreased primary air in the second stage, which slows the flow speed of combustible gases released from the bed and allows the secondary air to push these gases more effectively toward the front of the furnace, enhancing gas-phase combustion and strengthening radiation intensity above the first stage. There is no significant change in the overall length and distribution of the fire bed, which is not reiterated here. Notably, as shown in Figure 13b, the delayed arrangement of primary air results in the depletion of O_2 in the front channel, while significantly increasing O_2 in the rear channel. Correspondingly, CO mainly enters the front channel. This creates a counterflow arrangement with a reductive atmosphere

https://doi.org/10.1021/acsomega.4c07041
ACS Omega 2024, 9, 42010−42026

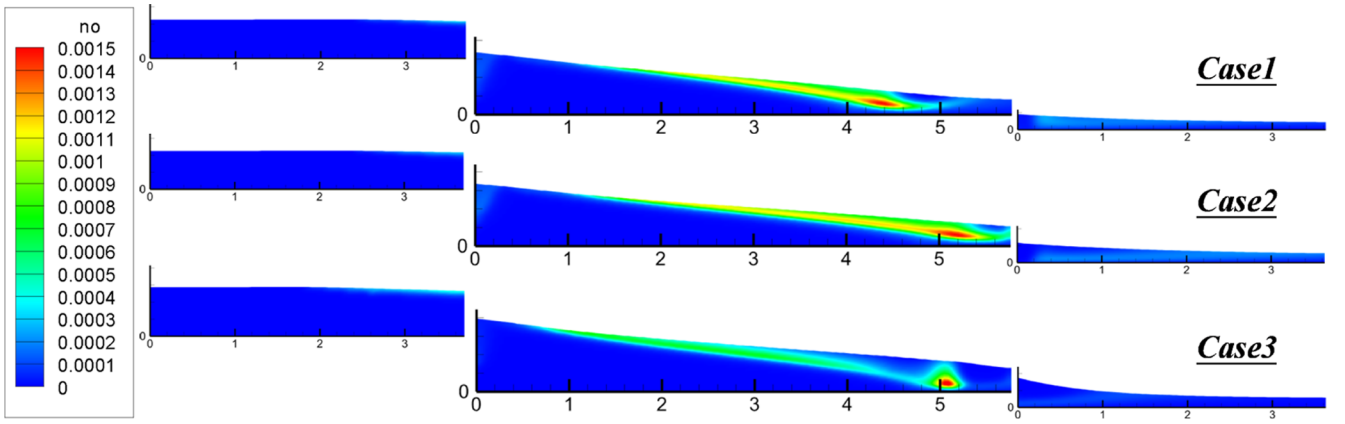

(a) Contour of mass fraction of NO

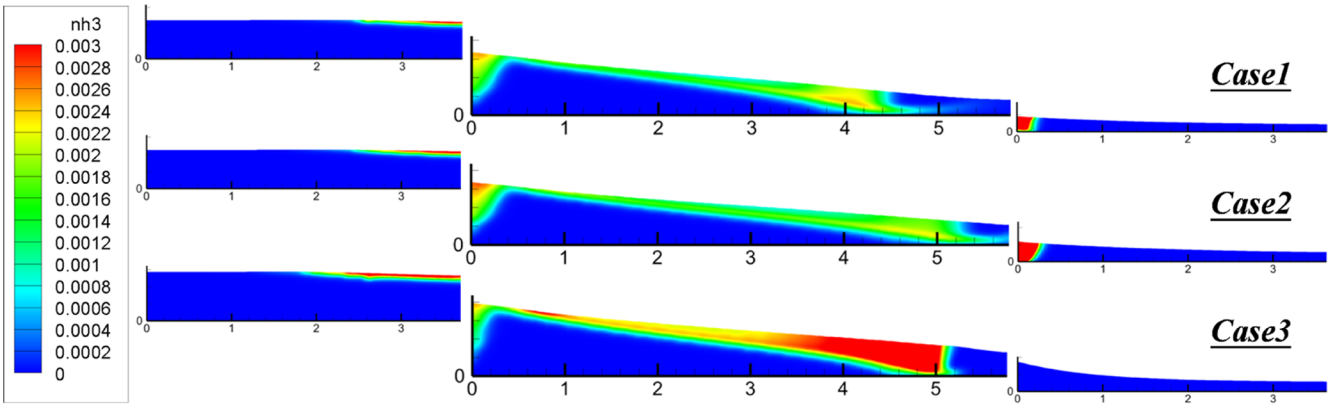

(b) Contour of mass fraction of NH_3

Figure 14. Distributions of NO and NH_3 in the bed before and after the two steps of adjustments.

in the horizontal front channel and an oxidative atmosphere in the rear channel, which are conducive to strengthening gas-phase combustion and inhibiting the emissions of CO and dioxins.

The control of NO_x emission is the main purpose of this step of adjustment, and the distributions of NO and NH_3 in the bed before and after the two steps of adjustments are compared in Figure 14. It is evident that, from case 1 to case 2, the reduction in the total amount of primary air makes the flame propagation process cover a longer length of the bed, and accordingly, the ranges of the release of both NO (see Figure 14a) and NH_3 (see Figure 14b) are significantly expanded. From case 2 to case 3, the changes in the distribution ratio of primary air in the three stages of the bed significantly reduce the amount of NO generated in the second stage during the flame propagation process and also greatly increase the amount of NH_3 at the top surface of the bed.

In order to quantitatively compare the changes in the release of NO and NH_3 from the bed after adjusting the distribution of primary air, Figure 15 summarizes the mass flow rates of NO and NH_3 at the bed surface under three conditions.

The comparison shows that values of the first NH_3 peaks in three cases, when the bed is ignited and flame propagation starts, are close. However, during the flame propagation

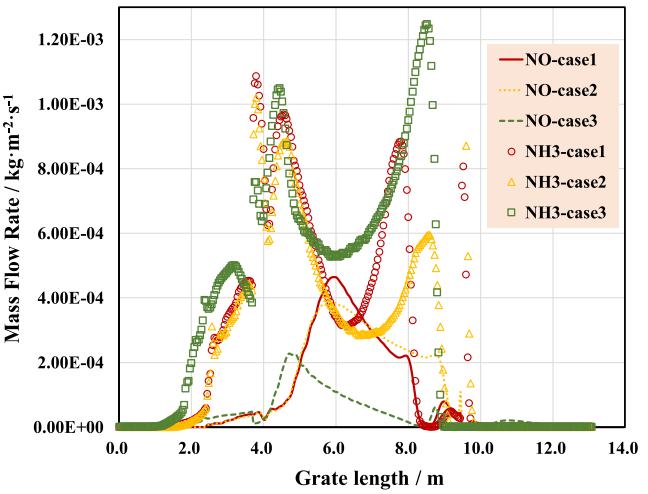

Figure 15. Distribution of NO and NH_3 at the top surface of the bed after primary air distribution was adjusted.

process, the case 3 scenario, which involves both a reduction in the total amount of primary air and a delayed air distribution, shows a significantly smaller decrease in NH_3 than case 1 and case 2. Correspondingly, with the reduction of primary air in the combustion stage, the peak value of NO in case 3 is about

https://doi.org/10.1021/acsomega.4c07041
ACS Omega 2024, 9, 42010−42026

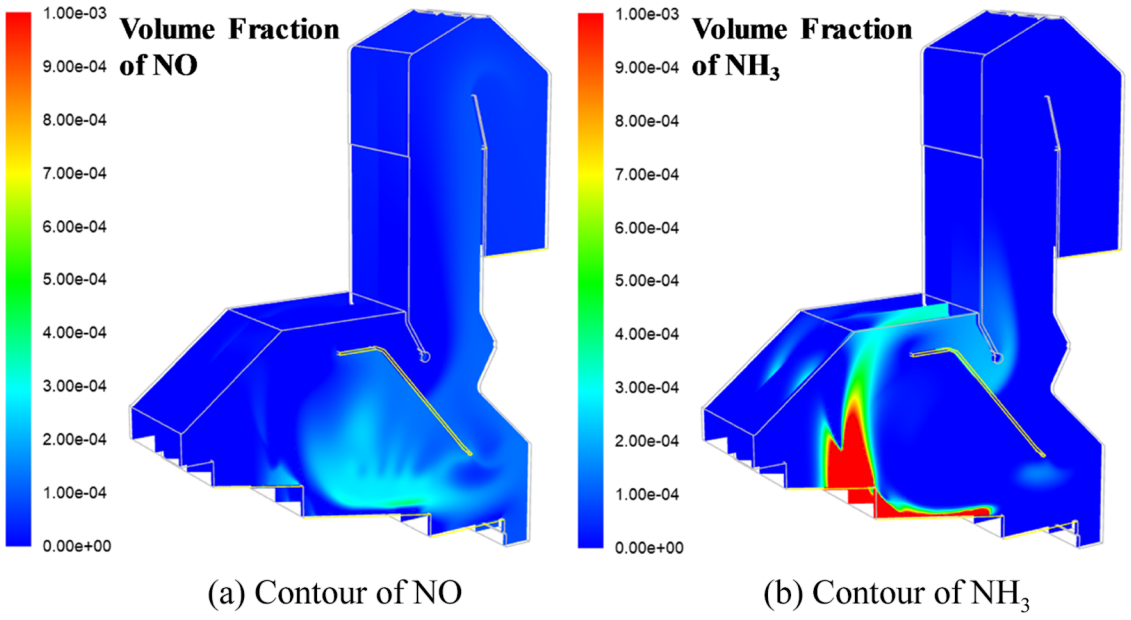

Figure 16. Distribution of NO and NH_3 in freeboard after primary air distribution was adjusted.

50% lower than cases 1 and case 2. Moreover, the ratio of NO to NH_3 at the top surface of bed is important. In case 1, the mass flow rate of NO at 6.0 m is clearly larger than NH_3, leading to the concentrated flow of NO in the freeboard. In case 2, although the difference between the mass flow rates of NO and NH_3 is getting close, still NO is larger. In case 3, the ratio of NO to NH_3 is completely changed. At this position, the mass flow rate of NO is about 1.0×10^{-4} kg/(m^2·s), and its maximum in the entire bed surface is only 2.2×10^{-4} kg/(m^2·s), while the minimum mass flow rate of NH_3 within the range exceeded 5.2×10^{-4} kg/(m^2·s). The reasons for these differences are 2-fold: first, the reduced supply of primary air limits the oxidation of NH_3 to NO; second, the higher bed provides a suitable environment for the reduction of NO by NH_3 and char. In summary, under this operating mode, the mass flow rate of NH_3 at the bed surface far exceeds that of NO, creating an optimal foundation for the reduction of NO in the freeboard.

The distribution of NO and NH_3 in the freeboard is presented in Figure 16. Due to the effective suppression of NO and the promotion of NH_3 within the fuel bed, the concentration of NO near the bed surface has decreased to a very low level compared to case 1 and case 2. As discussed above, after adjustment of the primary air distribution, it forms a reductive atmosphere in the horizontal front channel and an oxidative atmosphere in the rear channel. Under this distribution, a large proportion of the NH_3 released from bed is retained and, together with combustible gases like CO, enters the vertical first flue via the horizontal front channel. On the rear side of the middle arch, a portion of NH_3 reacts with O_2 producing NO, but at the same time, it reacts with the formed NO to reduce it, resulting in a limited overall production of NO in the competitive reactions. The produced NO then enters the vertical first flue with O_2 and combustion products via the rear channel. The NH_3 predominating in the front channel and NO predominating in the rear channel mix at the bottom of the vertical first flue and further undergo NO reduction reactions. Under these conditions, the volume fraction of the O_2 at the boiler outlet is 3.26%, and the original emission concentration of NO_x is only 95.94 mg/(N·m^3), which can achieve an emission concentration of 50 mg/(N·m^3) with only SNCR.

Based on this optimization scenario, adjustment and verification are conducted on the actual furnace in the waste incineration plant. Following the configurations of case 3, the total amount of primary air is gradually reduced, and the secondary air is simultaneously increased to bring their ratio close to 6:4, while maintaining the oxygen concentration at the furnace exit at around 4%. Additionally, adjustments are made to the valves of the air chambers of the three stages according to the on-site bed combustion condition and the location of the fire bed, gradually reducing the proportion of primary air in the second stage and moderately delaying the air supply. Finally, the movement speed of the bed on the grate is reduced to increase the thickness of the bed. After all adjustments are completed, the incinerator gradually approaches a stable combustion state.

Figure 17 shows photographs of the bed combustion taken from the rear arch, where it is evident that after operational adjustments the fire bed is extended. The structure at the top of the photograph is the back end of the middle arch. Under common operation conditions, bed combustion is more likely to concentrate in the front part of the grate, with the flame mainly in front of the back end of the middle arch. After adjustments, the extension of bed combustion led to a significant amount of volatile combusting in the rear of the middle arch and flowing into the vertical first flue via the rear channel, consistent with the trends predicted by numerical simulation.

Regarding the localized high-temperature issues in the horizontal front channel and the vertical first flue, Figure 18 compares the temperature distribution in the freeboard under common operation conditions (Figure 18a) and after adjustments (Figure 18b). The panel data shows that the temperatures at the measurement points in the horizontal front channel and the vertical first flue have significantly decreased after the adjustments, effectively solving the previous local overheating problems, which is also in good agreement

https://doi.org/10.1021/acsomega.4c07041
ACS Omega 2024, 9, 42010−42026

Figure 17. Photographs of the bed combustion taken from the rear arch.

with the numerical simulation prediction. As presented in the simulation results in Figure 13, the reduction in the temperature of the horizontal front channel is mainly due to the organization of volatile combustion in a lower area beneath the middle arch, while it is mainly reductive gases that pass the front channel. As for the first flue, the double channels formed by the middle arch create counterflow mixing and reaction between combustible gases and oxygen, resulting in a more even temperature distribution within it and preventing the localized high-temperature problem. Mitigating the local overheating and slagging problems not only improves operational efficiency but also extends the lifespan of incinerator components. This reduction in maintenance needs also contributes to environmental sustainability by lowering raw material consumption as well as associated environmental impacts of manufacturing and transportation.

Lastly, concerning the control effect of NO_x, Figure 19 shows the changes in the NO_x emission concentration (11% O_2) and boiler load during the adjustment process. Before the adjustment, the emission concentration of NO_x is around 200 mg/(N·m^3). With the completion of the adjustment action, the NO_x emission concentration rapidly decreased and eventually

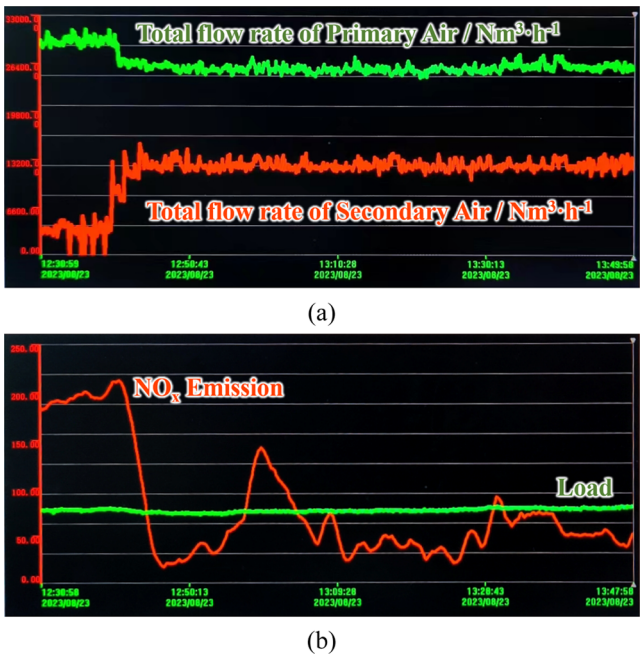

Figure 19. NO_x emission concentration (b, red line) and boiler load (b, green line) during the adjustments in primary and secondary air (a).

stabilized at around 50 mg/(N·m^3). Throughout the entire adjustment process, the boiler load remained relatively stable. Considering the deployment of NO_x control measures such as SNCR, the on-site control effect of NO_x is consistent with the numerical simulation, predicting an original NO_x concentration of 95.94 mg/(N·m^3). This 75% decrease in the NO_x emission, from 200 to 50 mg/(N·m^3), substantially lowers the incinerator's contribution to air pollution, mitigating potential health risks and environmental damage associated with NO_x, such as acid rain formation and ground-level ozone production.

In summary, based on the optimization scenario designed by numerical simulation, the operational adjustments to the middle-arch incinerator solved local overheating problems at different positions, significantly reduced NO_x emission, and

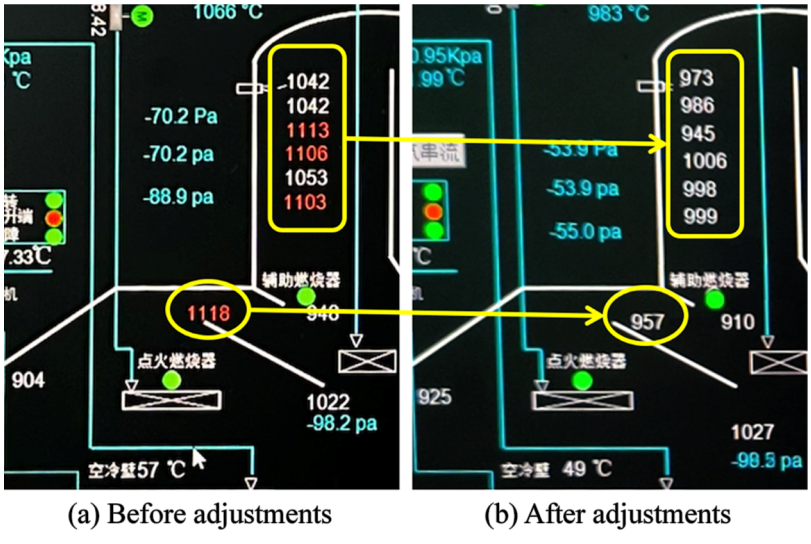

Figure 18. Comparison of the temperature distribution in freeboard before (a) and after (b) adjustments.

https://doi.org/10.1021/acsomega.4c07041
ACS Omega 2024, 9, 42010−42026

nearly had a negative effect on boiler load, achieving the expected and predicted optimization results.

5. CONCLUSIONS

This study developed a comprehensive model for municipal solid waste (MSW) incineration by coupling a multiphase fuel bed model with a 3D furnace combustion model. The fuel bed model, incorporating a thermally thick particle treatment, enabled detailed analysis of furnace temperature, component distribution, and flow field dynamics. The key findings are presented as follows.

(1) Numerical simulation and analysis of the common conditions of the incinerator were carried out, concerning the localized high temperatures and elevated NO_x emission. Major contributors to these issues were identified, including an imbalanced ratio of primary to secondary air, excessively rapid flame propagation and concentrated volatile release in the bed, and poor component mixing and distribution in the freeboard.

(2) Based on the simulation and evaluation of the effects of operation parameters, effective mitigation strategies were developed to address these issues, involving reduction of the proportion of primary air while increasing secondary air, adjustment of the distribution of primary air in three stages with delayed supply toward the burnout stage, decrease in grate move speed to create a thick-bed combustion mode, and enhancement in the counterflow mixing of NH_3 and NO at the bottom of first flue.

(3) Through model-guided adjustments, significant improvements in incinerator performance were achieved. NO_x emissions were reduced from 200 mg/(N·m^3) to approximately 50 mg/(N·m^3). The temperature in the problematic horizontal front channel, which suffered from severe slagging, was lowered from 1118 to 957 °C. Importantly, these optimizations were achieved under a stable rated boiler load, demonstrating the effectiveness of the approach.

This research demonstrates the potential of advanced modeling techniques to optimize MSW incinerator design and operation. The findings offer practical solutions for reducing environmental impact and improving operational efficiency in waste incineration facilities.

AUTHOR INFORMATION

Corresponding Author

Ruizhi Zhang − *Institute of Thermal Energy Engineering, School of Mechanical Engineering, Shanghai Jiao Tong University, Shanghai 200240, China;* orcid.org/0000-0002-8136-3529; Email: zhang.ruizhi@sjtu.edu.cn

Authors

Hongquan Zhou − *Thermal Environmental Engineering Institute, Tongji University, Shanghai 200092, China; Shanghai Environmental Sanitation Engineering Design Institute Co., Ltd, Shanghai 200232, China*

Linzheng Wang − *Institute of Thermal Energy Engineering, School of Mechanical Engineering, Shanghai Jiao Tong University, Shanghai 200240, China*

Yonghao Luo − *Institute of Thermal Energy Engineering, School of Mechanical Engineering, Shanghai Jiao Tong University, Shanghai 200240, China;* orcid.org/0000-0002-3281-9008

Complete contact information is available at: https://pubs.acs.org/10.1021/acsomega.4c07041

Author Contributions

H.Z.: On-site operational optimization of the MSW incinerator and writing-original draft. R.Z.: Modeling of the MSW incinerator and design and evaluation of the optimization strategy. L.W.: Modeling of the MSW incinerator and writing—review and editing. Y.L.: Conceptualization, methodology, and funding acquisition.

Notes

The authors declare no competing financial interest.

ACKNOWLEDGMENTS

The authors acknowledge the financial support from the National Natural Science Foundation of China [51706139] and the Science and Technology Commission of Shanghai Municipality [23DZ1201402].

REFERENCES

(1) Han, X.; Chang, H.; Wang, C.; Tai, J.; Karellas, S.; Yan, J.; Song, L.; Bi, Z. Tracking the Life-Cycle Greenhouse Gas Emissions of Municipal Solid Waste Incineration Power Plant: A Case Study in Shanghai. *J. Cleaner Prod.* **2023**, *398*, No. 136635.

(2) Oviedo-Ocaña, E.; Abendroth, C.; Domínguez, I. C.; Sánchez, A.; Dornack, C. Life Cycle Assessment of Biowaste and Green Waste Composting Systems: A Review of Applications and Implementation Challenges. *Waste Manage.* **2023**, *171*, 350−364.

(3) Luo, Z.; Chen, W.; Wang, Y.; Cheng, Q.; Yuan, X.; Li, Z.; Yang, J. Numerical Simulation of Combustion and Characteristics of Fly Ash and Slag in a "V-Type" Waste Incinerator. *Energies* **2021**, *14* (22), 7518.

(4) Makarichi, L.; Jutidamrongphan, W.; Techato, K. The Evolution of Waste-to-Energy Incineration: A Review. *Renewable Sustainable Energy Rev.* **2018**, *91*, 812−821.

(5) Fu, Z.; Lin, S.; Tian, H.; Hao, Y.; Wu, B.; Liu, S.; Luo, L.; Bai, X.; Guo, Z.; Lv, Y. A Comprehensive Emission Inventory of Hazardous Air Pollutants from Municipal Solid Waste Incineration in China. *Sci. Total Environ.* **2022**, *826*, No. 154212.

(6) Hu, Z.; Jiang, E.; Ma, X. Numerical Simulation on NOX Emissions in a Municipal Solid Waste Incinerator. *J. Cleaner Prod.* **2019**, *233*, 650−664.

(7) Yang, X.; Liao, Y.; Ma, X.; Zhou, J. Effects of Air Supply Optimization on NOx Reduction in a Structurally Modified Municipal Solid Waste Incinerator. *Appl. Therm. Eng.* **2022**, *201*, No. 117706.

(8) Yang, X.; Liao, Y.; Wang, Y.; Chen, X.; Ma, X. Research of Coupling Technologies on NOx Reduction in a Municipal Solid Waste Incinerator. *Fuel* **2022**, *314*, No. 122769.

(9) Zeng, W.; Wang, Y.; Bu, Q.; Ma, S.; Hu, H.; Ma, D.; Ma, H. Influence of Main Operating Parameters on the Incineration Characteristics of Municipal Solid Waste (MSW). *Process Saf. Environ. Prot.* **2024**, *185*, 325−339.

(10) Zhuang, J.; Tang, J.; Aljerf, L. Comprehensive Review on Mechanism Analysis and Numerical Simulation of Municipal Solid Waste Incineration Process Based on Mechanical Grate. *Fuel* **2022**, *320*, No. 123826.

(11) Liang, Y.; Tang, J.; Xia, H.; Aljerf, L.; Gao, B.; Akele, M. L. Three-Dimensional Numerical Modeling and Analysis for the Municipal Solid-Waste Incineration of the Grate Furnace for Particulate-Matter Generation. *Sustainability* **2023**, *15* (16), 12337.

(12) Xia, Z.; Shan, P.; Chen, C.; Du, H.; Huang, J.; Bai, L. A Two-Fluid Model Simulation of an Industrial Moving Grate Waste Incinerator. *Waste Manage.* **2020**, *104*, 183−191.

(13) Yan, M.; Tian, X.; Antoni; Yu, C.; Zhou, Z.; Hantoko, D.; Kanchanatip, E.; Khan, M. S. Influence of Multi-Temperature Primary Air on the Characteristics of MSW Combustion in a Moving Grate Incinerator. *J. Environ. Chem. Eng.* **2021**, *9* (6), No. 106690.

(14) Qi, X.; Ma, X.; Yu, Z.; Huang, Z.; Teng, W. Numerical Simulation of Municipal Waste and Food Digestate Blending Combustion and NOx Reduction under Oxygen-Enriched Atmospheres. *Fuel* **2023**, *345*, No. 128115.
(15) Iwasaki, T.; Nakayama, T.; Denda, T.; Kinoshita, S.; Nakagawa, T.; Ayukawa, S. Advance in Waste Incineration Technology. *J. Combust. Soc. Jpn.* **2011**, *53* (164), 85−90.
(16) Hoang, Q. N.; Vanierschot, M.; Blondeau, J.; Croymans, T.; Pittoors, R.; Van Caneghem, J. Review of Numerical Studies on Thermal Treatment of Municipal Solid Waste in Packed Bed Combustion. *Fuel Commun.* **2021**, *7*, No. 100013.
(17) Gómez, M.; Porteiro, J.; Patiño, D.; Míguez, J. L. CFD Modelling of Thermal Conversion and Packed Bed Compaction in Biomass Combustion. *Fuel* **2014**, *117*, 716−732.
(18) Wang, L.; Zhang, R.; Deng, R.; Liu, Z.; Luo, Y. Comprehensive Parametric Study of Fixed-Bed Co-Gasification Process through Multiple Thermally Thick Particle (MTTP) Model. *Appl. Energy* **2023**, *348*, No. 121525.
(19) Deng, R.; Wang, L.; Zhang, R.; Luo, Y. Numerical Modeling of Fixed-Bed Cocombustion Processes through the Multiple Thermally Thick Particle Model. *ACS Omega* **2022**, *7* (44), 39938−39949.
(20) Zhang, R.; Wang, L.; Deng, R.; Luo, Y. Numerical Analysis of NO_x Reduction in Large-Scale MSW Grate Furnace through in-Bed Combustion Optimization Using Multi-Section Fuel Bed Model with Thermally Thick Treatment. *Appl. Therm. Eng.* **2024**, *257*, No. 124156.
(21) Yang, Y. B.; Lim, C. N.; Goodfellow, J.; Sharifi, V. N.; Swithenbank, J. A Diffusion Model for Particle Mixing in a Packed Bed of Burning Solids. *Fuel* **2005**, *84* (2−3), 213−225.
(22) Nakamura, M. R.; Castaldi, M. J.; Themelis, N. J. Stochastic and Physical Modeling of Motion of Municipal Solid Waste (MSW) Particles on a Waste-to-Energy (WTE) Moving Grate. *Int. J. Therm. Sci.* **2010**, *49* (6), 984−992.
(23) Ma, W.; Ma, C.; Liu, X.; Gu, T.; Thengane, S. K.; Bourtsalas, A.; Chen, G. Nox Formation in Fixed-Bed Biomass Combustion: Chemistry and Modeling. *Fuel* **2021**, *290*, No. 119694.
(24) Gómez, M.; Porteiro, J.; Patiño, D.; Míguez, J. L. Fast-Solving Thermally Thick Model of Biomass Particles Embedded in a CFD Code for the Simulation of Fixed-Bed Burners. *Energy Convers. Manage.* **2015**, *105*, 30−44.
(25) Lin, K.-S.; Wang, H. P.; Liu, S.-H.; Chang, N.-B.; Huang, Y.-J.; Wang, H.-C. Pyrolysis Kinetics of Refuse-Derived Fuel. *Fuel Process. Technol.* **1999**, *60* (2), 103−110.
(26) Ngamsidhiphongsa, N.; Ponpesh, P.; Shotipruk, A.; Arpornwichanop, A. Analysis of the Imbert Downdraft Gasifier Using a Species-Transport CFD Model Including Tar-Cracking Reactions. *Energy Convers. Manage.* **2020**, *213*, No. 112808.
(27) Li, Y.; Hong, C.; Wang, Y.; Xing, Y.; Chang, X.; Zheng, Z.; Li, Z.; Zhao, X. Nitrogen Migration Mechanism during Pyrolysis of Penicillin Fermentation Residue Based on Product Characteristics and Quantum Chemical Analysis. *ACS Sustainable Chem. Eng.* **2020**, *8* (20), 7721−7740.
(28) Chen, W.; Yang, H.; Chen, Y.; Xia, M.; Chen, X.; Chen, H. Transformation of Nitrogen and Evolution of N-Containing Species during Algae Pyrolysis. *Environ. Sci. Technol.* **2017**, *51* (11), 6570−6579.
(29) Zhan, H.; Yin, X.; Huang, Y.; Yuan, H.; Wu, C. NO Precursors Evolving during Rapid Pyrolysis of Lignocellulosic Industrial Biomass Wastes. *Fuel* **2017**, *207*, 438−448.
(30) Ulusoy, B.; Lin, W.; Karlström, O.; Li, S.; Song, W.; Glarborg, P.; Dam-Johansen, K.; Wu, H. Formation of NO and N_2O during Raw and Demineralized Biomass Char Combustion. *Energy Fuels* **2019**, *33* (6), 5304−5315.
(31) Porteiro, J.; Patiño, D.; Moran, J.; Granada, E. Study of a Fixed-Bed Biomass Combustor: Influential Parameters on Ignition Front Propagation Using Parametric Analysis. *Energy Fuels* **2010**, *24* (7), 3890−3897.

https://doi.org/10.1021/acsomega.4c07041
ACS Omega 2024, 9, 42010−42026